PERGAMON

International Journal of Solids and Structures 37 (2000) 2951–2980

INTERNATIONAL JOURNAL OF SOLIDS and STRUCTURES

www.elsevier.com/locate/ijsolstr

Large-deformation tests and total-Lagrangian finite-element analyses of flexible beams

P. Frank Pai[a,*], Tony J. Anderson[b], Eric A. Wheater[c]

[a]*Department of Mechanical and Aerospace Engineering, University of Missouri, Columbia, MO 65211, USA*
[b]*Department of Mechanical Engineering, University of Idaho, Moscow, ID 83844, USA*
[c]*Department of Mechanical Engineering, North Carolina A&T State University, Greensboro, NC 27411, USA*

Received 23 June 1998; received in revised form 1 April 1999

Abstract

Presented here is a total-Lagrangian displacement-based finite-element formulation for general anisotropic beams undergoing large displacements and rotations. The theory fully accounts for geometric nonlinearities (large rotations), general initial curvatures, and extensionality by using Jaumann stress and strain measures, an exact coordinate transformation, and a new concept of orthogonal virtual rotations. Moreover, transverse shear deformations are accounted for by using a first-order shear-deformation theory. To verify the accuracy of the finite-element model, two test fixtures have been built for bending and twisting experiments. Large static deformation tests of beams with different loading conditions have been performed. The finite-element results agree closely with the experimental results and numerically exact solutions obtained by using a multiple shooting method to solve for post-buckling deformations of highly flexible beams undergoing large static rotations and displacements in three-dimensional space.

Keywords: Total-Lagrangian beam theory; Finite elements; Large-deformation tests

1. Introduction

Highly Flexible Structures (HFSs) have been used in many mechanical systems, civil structures, and aerospace vehicles to satisfy space limitations, provide special mechanisms, and/or reduce structural weight. Moreover, because current NASA space missions require structures that have dimensions much greater than the shroud diameter of launch vehicles, deployable HFSs are extensively used in space structures. This extensive use of HFSs reveals the need for a design and analysis software and a database system with guidelines for designing HFSs.

* Corresponding author Tel.: +001-573-884-1474; Fax: +001-573-884-5090.
E-mail address: paip@missouri.edu (P.F. Pai).

0020-7683/00/$ - see front matter
PII: S0020-7683(99)00115-8

In analyzing geometrically nonlinear structures, a Lagrangian formulation is commonly used because there is a natural undeformed state to which the body would return when it is unloaded. Moreover, because the structural stiffnesses of such systems are functions of displacements, an incremental/iterative procedure is commonly used in solving such problems. Approaches used in the literature in geometrically nonlinear finite-element analysis can be grouped into four:

1. an Updated Lagrangian (UL) formulation using linear strains (e.g., engineering strains) defined with respect to the deformed configuration,
2. an UL-formulation using truncated nonlinear strain–displacement relations (e.g., von Karman strains),
3. a Total Lagrangian (TL) formulation using fully nonlinear strain–displacement relations (e.g., Green–Lagrange strains) derived by using large rotational Degrees Of Freedom (DOFs), and
4. a TL-formulation using fully or truncated nonlinear strain–displacement relations (e.g., Green–Lagrange strains) defined with respect to a corotated elemental reference frame.

In an UL-formulation, the referential geometry (i.e., volume, area, coordinates) is brought up-to-date at every incremental step upon convergence but fixed during the iterative process. Such an UL-formulation may be regarded as an application of the TL-formulation to a single load step with the previously converged configuration as an initial geometry. If an UL-formulation based on a linear strain–displacement relation is employed, the update process needs to be performed at every iteration (Lee, 1992). In an UL-formulation, the accuracy of current solutions in an incremental/iterative solution procedure is affected by the accuracy of solutions of the previous step, and the error of the updated configuration may accumulate when the number of steps increases. Moreover, the magnitude of incremental steps (load, displacement, or arc-length steps) needs to be infinitesimal (if linear strain–displacement relations are used) or small (if truncated nonlinear strain–displacement relations are used) because it is limited by convergence consideration and the method used in approximating large rotations (not vector quantities). Furthermore, because the deformed geometry is used as the reference frame in an UL-formulation, the obtained displacements, stresses, and strains need transformation before update, which is computationally expensive.

In a TL-formulation, the accuracy of current solutions is not affected by the accuracy of solutions obtained in the previous step, and the obtained displacements, stresses, and strains do not need transformation before update. Moreover, the incremental steps used in a TL-formulation are usually larger than those used in an UL-formulation because they are only limited by convergence consideration. Theoretically, if the solution converges, arbitrarily large steps can be used and no accuracy is lost in an incremental/iterative solution procedure using a TL-formulation. However, it is difficult to derive appropriate fully nonlinear strain–displacement relations. For a review of nonlinear beam theories, the reader is referred to the introduction section of Pai and Nayfeh (1994b).

Two approaches are commonly used in deriving fully nonlinear strain–displacement relations. The first one (used in Approach (3)) uses three or two large Euler-type rotation angles as well as three displacement DOFs with respect to the undeformed reference frame (Surana, 1983; Palazotto and Dennis, 1992). Since finite rotation angles are not vector quantities, the derived strain–displacement relation is not invariant with respect to the rotation sequence. Hence, this approach is not appropriate for bifurcation study because some solutions may be prevented from being obtained if multiple solutions exist. Moreover, since the large rotational DOFs are usually treated as independent DOFs although they are functions of derivatives of translational DOFs, the orders of interpolation functions for rotational DOFs may not be consistent with those of translational DOFs. This inconsistency may cause the occur of spurious strains. Moreover, some finite elements derived from this approach use lower order interpolation functions for in-plane displacements than those for the out-of-plane displacements. This can cause spurious strains too. The second approach (used in Approach (4)) is to use three or two small

Euler-type rotation angles or triads or quarternions as well as three displacement DOFs with respect to a corotated reference frame (Rankin and Brogan, 1986; Kohnke, 1989; Nygard and Bergan, 1989; Stanley and Nour-Omid, 1990).

Corotation is a method developed for making large rotations relative to an inertial frame look like small rotations at the element level (Nygard and Bergan, 1989). This is achieved by defining, for each element, a corotated element reference coordinate frame using the deformed nodal coordinates. The rigid body motion of this frame is then 'subtracted' from the total motion of the nodes, leaving relative translations and rotations that can be made arbitrarily small by simply refining the mesh. Once nodal relative motions have been rendered sufficiently small, the relative small rotations can be treated as vector quantities and they may be used in simplified strain–displacement relations. Nygard and Bergan (1989) proved that the values of Green strains (second Piola–Kirchhoff stresses) defined with respect to the undeformed frame are the same as those defined with respect to the corotated frame and hence there is no need of transformation before updating these strains and stresses. However, the global displacements need transformation before updating (Rankin and Brogan, 1986). Moreover, because the corotated frame is defined by nodal coordinates, the sizes of elements need to be small in order to keep the relative rotations small (Nygard and Bergan, 1989).

The above discussions show that a TL-formulation with corotation is the most attractive approach, and fully nonlinear or truncated Green–Lagrange strains are commonly used in this approach (Lee, 1992; Rankin and Brogan, 1986; Nygard and Bergan, 1989; Stanley and Nour-Omid, 1990). Nonlinear strains used in a TL-formulation need to be objective and geometric in order to use the material constants obtained from experiments in which rigid-body rotations are prevented and engineering stress and strain measures are used (Malvern, 1969; Pai and Nayfeh, 1994a). Unfortunately, Green–Lagrange strains are not geometric measures although they are objective (Pai and Nayfeh, 1994a; Pai and Palazotto, 1995a).

A total-Lagrangian finite-element code GESA (Geometrically Exact Structural Analysis) has been under development for analyzing highly flexible structures. GESA is a displacement-based finite-element code written in the MATLAB language and is based on theories developed for structures undergoing large displacements, large rotations, and finite strains (Pai and Nayfeh, 1991, 1992, 1994a, 1994b, 1994c; Pai and Palazotto, 1995a, 1995b; Pai, 1995; Pai and Schulz, 1999; Pai et al., 1998). The structural theories fully account for geometric nonlinearities due to large rotations, large in-plane strains of two-dimensional structures, large axial strains of one-dimensional structures, initial curvatures, and transverse shear deformations by using Jaumann stress and strain measures, an exact coordinate transformation, and a new concept of orthogonal virtual rotations. The Jaumann strains are derived using a new concept of local displacements without performing polar decomposition and they are proved to be a corotated geometric objective measure. A corotated point reference frame is defined using the symmetry of Jaumann strains. Moreover, there is no need for transformation before updating strains, stresses, and displacements.

This paper presents a total-Lagrangian formulation of beam elements, large static deformation test set-ups and experimental results, and numerical solutions from GESA.

2. Reference-line deformations

Deformation of a beam consists of its reference line deformation and the in-plane and out-of-plane warpings of its cross section with respect to the plane perpendicular to the deformed reference line. Different approximations of the reference line deformation result in different geometrically nonlinear beam theories. Different approximations of the out-of-plane warpings result in different shear-

deformable beam theories. In this section we show how to describe exactly the deformation of an initially curved and twisted reference line.

2.1. Coordinate transformations and curvatures

In the absence of in-plane and out-of-plane warpings, a differential beam element is a rigid thin 'plate' having an infinitesimal thickness and a fixed finite area and is perpendicular to the reference line before and after deformation. Hence, the motion of such a beam element can be described by three translational displacements and three rotations. As in rigid-body dynamics, three or two consecutive Euler angles can be used to describe the rotation of such a rigid 'plate' from the undeformed position to the deformed position.

We consider the initially curved and twisted beam depicted in Fig. 1. To describe the reference line deformation and the rotations of the observed rigid cross-section, two coordinate systems are needed; the system xyz describes the undeformed system configuration and the system $\xi\eta\zeta$ describes the deformed system configuration. The system xyz is an orthogonal curvilinear coordinate system in which the axis x is the reference line formed by connecting the reference points of all cross sections of the undeformed beam; and the system $\xi\eta\zeta$ is a local orthogonal curvilinear coordinate system in which the axis ξ represents the deformed reference line and the axes η and ζ represent the deformed configurations of the axes y and z with no cross-section warping. The system XYZ is a rectangular coordinate system used for reference purpose in the calculation of initial curvatures. We let $\mathbf{i}_a$, $\mathbf{i}_b$, and $\mathbf{i}_c$ denote the unit

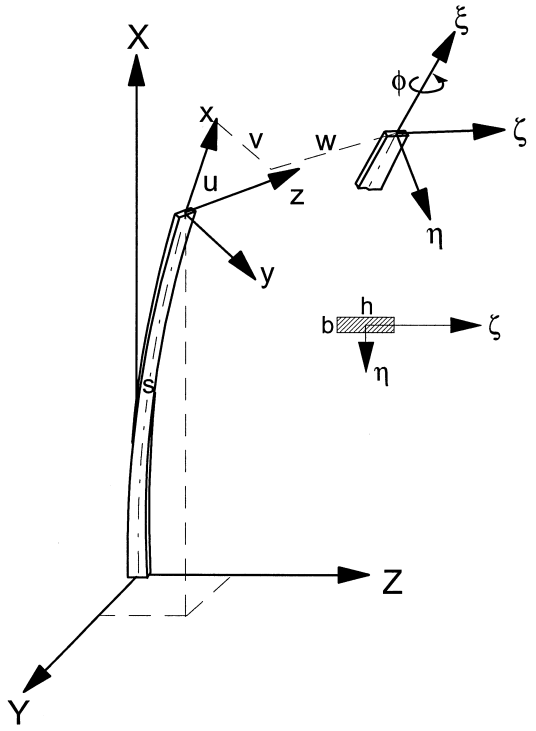

Fig. 1. Three coordinate systems are used in the modeling: XYZ is a rectangular coordinate system used for reference; xyz is an orthogonal curvilinear frame, where the x-axis represents the undeformed reference line; and $\xi\eta\zeta$ is an orthogonal curvilinear frame, where the ξ-axis represents the deformed reference line.

vectors of the system XYZ; $\mathbf{i}_x$, $\mathbf{i}_y$, and $\mathbf{i}_z$ denote the unit vectors of the system xyz; and $\mathbf{i}_1$, $\mathbf{i}_2$, and $\mathbf{i}_3$ denote the unit vectors of the system $\xi\eta\zeta$. Furthermore, s denotes the undeformed arc length along the axis x from the root of the beam to the observed element, and u, v and w represent the displacement components of the reference point (i.e., the origin of the system xyz) of the observed cross section with respect to the axes x, y, and z, respectively.

The undeformed position vector $\bar{\mathbf{R}}$ of the reference point of the observed cross section is assumed to be known and given by

$$\bar{\mathbf{R}} = A(s)\mathbf{i}_a + B(s)\mathbf{i}_b + C(s)\mathbf{i}_c. \tag{1}$$

Also, the angles θ_{21}, θ_{22} and θ_{23} of the y-axis with respect to the XYZ system are assumed to be known and given by

$$\theta_{21}(s) = \cos^{-1}(\mathbf{i}_y \cdot \mathbf{i}_a),\ \theta_{22}(s) = \cos^{-1}(\mathbf{i}_y \cdot \mathbf{i}_b),\ \theta_{23}(s) = \cos^{-1}(\mathbf{i}_y \cdot \mathbf{i}_c), \tag{2}$$

where $0 \le \theta_{2i} \le 180^\circ$. It follows from Eq. (1) that

$$\mathbf{i}_x = \bar{\mathbf{R}}' = A'\mathbf{i}_a + B'\mathbf{i}_b + C'\mathbf{i}_c, \tag{3}$$

where $(\,)' \equiv \partial(\,)/\partial s$. Using Eqs. (2) and (3) and the identity $\mathbf{i}_z = \mathbf{i}_x \times \mathbf{i}_y$, we obtain

$$\begin{Bmatrix} \mathbf{i}_x \\ \mathbf{i}_y \\ \mathbf{i}_z \end{Bmatrix} = [T^x] \begin{Bmatrix} \mathbf{i}_a \\ \mathbf{i}_b \\ \mathbf{i}_c \end{Bmatrix}, \tag{4}$$

where the transformation matrix $[T^x]$ is given by

$$[T^x(s)] = \begin{bmatrix} A' & B' & C' \\ \cos\theta_{21} & \cos\theta_{22} & \cos\theta_{23} \\ B'\cos\theta_{23} - C'\cos\theta_{22} & C'\cos\theta_{21} - A'\cos\theta_{23} & A'\cos\theta_{22} - B'\cos\theta_{21} \end{bmatrix}. \tag{5}$$

Using Eq. (4) and the orthonormality property of $\mathbf{i}_x$, $\mathbf{i}_y$, and $\mathbf{i}_z$ (e.g., $\mathbf{i}_x' \cdot \mathbf{i}_x = 0$ and $\mathbf{i}_x' \cdot \mathbf{i}_y = -\mathbf{i}_y' \cdot \mathbf{i}_x$), we obtain

$$\frac{\mathrm{d}}{\mathrm{d}s}\begin{Bmatrix} \mathbf{i}_x \\ \mathbf{i}_y \\ \mathbf{i}_z \end{Bmatrix} = [k]\begin{Bmatrix} \mathbf{i}_x \\ \mathbf{i}_y \\ \mathbf{i}_z \end{Bmatrix},\ [k] = \begin{bmatrix} 0 & k_3 & -k_2 \\ -k_3 & 0 & k_1 \\ k_2 & -k_1 & 0 \end{bmatrix}, \tag{6}$$

where k_1, k_2, and k_3 are the initial curvatures with respect to the axes x, y and z, respectively, and they are given by

$$k_1(s) = \frac{\mathrm{d}\mathbf{i}_y}{\mathrm{d}s} \cdot \mathbf{i}_z = \frac{\mathrm{d}T^x_{2i}}{\mathrm{d}s} T^x_{3i},\ k_2(s) = -\frac{\mathrm{d}\mathbf{i}_x}{\mathrm{d}s} \cdot \mathbf{i}_z = -\frac{\mathrm{d}T^x_{1i}}{\mathrm{d}s} T^x_{3i},\ k_3(s) = \frac{\mathrm{d}\mathbf{i}_x}{\mathrm{d}s} \cdot \mathbf{i}_y = \frac{\mathrm{d}T^x_{1i}}{\mathrm{d}s} T^x_{2i}. \tag{7}$$

In Eq. (7) and hereafter, unless otherwise stated, the repeated subscript indices imply summations.

Moreover, the deformed coordinate system $\xi\eta\zeta$ and the undeformed coordinate system xyz are related by the transformation matrix $[T]$ derived by using two Euler angles as (Alkire, 1984; Pai and Nayfeh, 1994b)

$$\begin{Bmatrix} \mathbf{i}_1 \\ \mathbf{i}_2 \\ \mathbf{i}_3 \end{Bmatrix} = [T]\begin{Bmatrix} \mathbf{i}_x \\ \mathbf{i}_y \\ \mathbf{i}_z \end{Bmatrix},\ [T] \equiv \begin{bmatrix} T_{11} & T_{12} & T_{13} \\ T_{21} & T_{22} & T_{23} \\ T_{31} & T_{32} & T_{33} \end{bmatrix}, \tag{8}$$

where

$$[T]=\begin{bmatrix}1 & 0 & 0\\ 0 & \cos\phi & \sin\phi\\ 0 & -\sin\phi & \cos\phi\end{bmatrix}\begin{bmatrix}T_{11} & T_{12} & T_{13}\\ -T_{12} & T_{11}+T_{13}^2/(1+T_{11}) & -T_{12}T_{13}/(1+T_{11})\\ -T_{13} & -T_{12}T_{13}/(1+T_{11}) & T_{11}+T_{12}^2/(1+T_{11})\end{bmatrix} \tag{9}$$

$$T_{11}=\frac{1+u'-vk_3+wk_2}{1+e},\ T_{12}=\frac{v'+uk_3-wk_1}{1+e},\ T_{13}=\frac{w'-uk_2+vk_1}{1+e} \tag{10}$$

$$e=\sqrt{(1+u'-vk_3+wk_2)^2+(v'+uk_3-wk_1)^2+(w'-uk_2+vk_1)^2}-1. \tag{11}$$

Here, e is the axial strain along the axis ξ, and ϕ is an Euler angle (see Fig. 1) related to the twisting with respect to the deformed reference axis ξ (Alkire, 1984; Pai and Nayfeh, 1994b). It follows from Eqs. (8) and (9) that T_{2i} and T_{3i} can be represented in terms of T_{11}, T_{12}, T_{13} and ϕ as

$$T_{21}=-\cos\phi T_{12}-\sin\phi T_{13},$$

$$T_{22}=\cos\phi\left(T_{11}+\frac{T_{13}^2}{1+T_{11}}\right)-\sin\phi\frac{T_{12}T_{13}}{1+T_{11}},$$

$$T_{23}=\sin\phi\left(T_{11}+\frac{T_{12}^2}{1+T_{11}}\right)-\cos\phi\frac{T_{12}T_{13}}{1+T_{11}},$$

$$T_{31}=\sin\phi T_{12}-\cos\phi T_{13},$$

$$T_{32}=-\sin\phi\left(T_{11}+\frac{T_{13}^2}{1+T_{11}}\right)-\cos\phi\frac{T_{12}T_{13}}{1+T_{11}}$$

$$T_{33}=\cos\phi\left(T_{11}+\frac{T_{12}^2}{1+T_{11}}\right)+\sin\phi\frac{T_{12}T_{13}}{1+T_{11}} \tag{12}$$

Differentiating Eq. (8) with respect to s and using Eq. (6) and the identity $[T]^T=[T]^{-1}$, we obtain

$$\frac{\partial}{\partial s}\begin{Bmatrix}\mathbf{i}_1\\ \mathbf{i}_2\\ \mathbf{i}_3\end{Bmatrix}=[K]\begin{Bmatrix}\mathbf{i}_1\\ \mathbf{i}_2\\ \mathbf{i}_3\end{Bmatrix}, \tag{13a}$$

$$[K]\equiv\begin{bmatrix}0 & \rho_3 & -\rho_2\\ -\rho_3 & 0 & \rho_1\\ \rho_2 & -\rho_1 & 0\end{bmatrix}=[T]'[T]^T+[T][k][T]^T, \tag{13b}$$

where ρ_1 is the deformed twisting curvature, and ρ_2 and ρ_3 are the deformed bending curvatures with respect to the system $\xi\eta\zeta$. They are obtained as

$$\rho_1 \equiv \mathbf{i}_2' \cdot \mathbf{i}_3 = T_{2i}' T_{3i} + T_{1i} k_i$$

$$= \phi' + \frac{1}{(1+e)(1+T_{11})}\Big[T_{13}\big(v' + k_3 u - k_1 w\big)' - T_{12}\big(w' - k_2 u + k_1 v\big)'\Big] + T_{1i} k_i,$$

$$\rho_2 \equiv -\mathbf{i}_1' \cdot \mathbf{i}_3 = -T_{1i}' T_{3i} + T_{2i} k_i$$

$$= \frac{-1}{1+e}\Big[T_{31}\big(u' - k_3 v + k_2 w\big)' + T_{32}\big(v' + k_3 u - k_1 w\big)' + T_{33}\big(w' - k_2 u + k_1 v\big)'\Big] + T_{2i} k_i$$

$$\rho_3 \equiv \mathbf{i}_1' \cdot \mathbf{i}_2 = T_{1i}' T_{2i} + T_{3i} k_i$$

$$= \frac{1}{1+e}\Big[T_{21}\big(u' - k_3 v + k_2 w\big)' + T_{22}\big(v' + k_3 u - k_1 w\big)' + T_{23}\big(w' - k_2 u + k_1 v\big)'\Big] + T_{3i} k_i, \tag{14}$$

where the orthogonality conditions, $T_{mi} T_{ni} = 0$, $m \neq n$, are used.

2.2. Orthogonal virtual rotations

To derive a set of governing equations describing motions along three perpendicular directions, the concept of orthogonal virtual rotations needs to be introduced. When large deformations are involved, curvatures are nonlinear functions of displacements and their spatial derivatives. Thus, to represent variations of curvatures in terms of variations of displacements and their derivatives, orthogonal virtual rotations are also needed. Variations of the unit vectors $\mathbf{i}_1$, $\mathbf{i}_2$ and $\mathbf{i}_3$ are due to virtual rigid-body rotations of the coordinate system $\xi\eta\zeta$ and are given by

$$\begin{Bmatrix} \delta\mathbf{i}_1 \\ \delta\mathbf{i}_2 \\ \delta\mathbf{i}_3 \end{Bmatrix} = \begin{bmatrix} 0 & \delta\theta_3 & -\delta\theta_2 \\ -\delta\theta_3 & 0 & \delta\theta_1 \\ \delta\theta_2 & -\delta\theta_1 & 0 \end{bmatrix} \begin{Bmatrix} \mathbf{i}_1 \\ \mathbf{i}_2 \\ \mathbf{i}_3 \end{Bmatrix}, \tag{15}$$

where $\delta\theta_1$, $\delta\theta_2$ and $\delta\theta_3$ are virtual rigid-body rotations with respect to the axes ξ, η and ζ, respectively. We note that $\delta\theta_i$ are infinitesimal rotations and hence they are vector quantities. Moreover, $\delta\theta_i$ are along three perpendicular directions and hence they are mutually independent. Using Eqs. (15), (8), (10) and (12), we obtain that

$$\delta\theta_1 = \delta\mathbf{i}_2 \cdot \mathbf{i}_3$$

$$= \delta\phi + \frac{T_{13}k_3 + T_{12}k_2}{1 + e + T_{11} + eT_{11}}\delta u - \frac{T_{12}k_1}{1 + e + T_{11} + eT_{11}}\delta v - \frac{T_{13}k_1}{1 + e + T_{11} + eT_{11}}\delta w$$

$$+ \frac{T_{13}}{1 + e + T_{11} + eT_{11}}\delta v' - \frac{T_{12}}{1 + e + T_{11} + eT_{11}}\delta w',$$

$$\delta\theta_2 = -\delta\mathbf{i}_1 \cdot \mathbf{i}_3$$

$$= \frac{T_{33}k_2 - T_{32}k_3}{1+e}\delta u + \frac{T_{31}k_3 - T_{33}k_1}{1+e}\delta v + \frac{T_{32}k_1 - T_{31}k_2}{1+e}\delta w - \frac{T_{31}}{1+e}\delta u' - \frac{T_{32}}{1+e}\delta v' - \frac{T_{33}}{1+e}\delta w'$$

$$\delta\theta_3 = \delta\mathbf{i}_1 \cdot \mathbf{i}_2$$

$$= \frac{T_{22}k_3 - T_{23}k_2}{1+e}\delta u + \frac{T_{23}k_1 - T_{21}k_3}{1+e}\delta v + \frac{T_{21}k_2 - T_{22}k_1}{1+e}\delta w + \frac{T_{21}}{1+e}\delta u' + \frac{T_{22}}{1+e}\delta v' + \frac{T_{23}}{1+e}\delta w'. \tag{16}$$

2.3. Variation of axial strain and curvatures

It follows from Eqs. (11) and (10) that

$$\delta e = T_{11}\big(\delta u' - k_3\delta v + k_2\delta w\big) + T_{12}\big(\delta v' + k_3\delta u - k_1\delta w\big) + T_{13}\big(\delta w' - k_2\delta u + k_1\delta v\big). \tag{17}$$

Taking the variations of Eq. (14) and using $\delta\mathbf{i}_k' = (\delta\mathbf{i}_k)'$ and Eqs. (15), (13a) and (13b), we obtain that

$$\delta\rho_1 = (\delta\theta_1)' - \rho_3\delta\theta_2 + \rho_2\delta\theta_3,$$

$$\delta\rho_2 = (\delta\theta_2)' + \rho_3\delta\theta_1 - \rho_1\delta\theta_3$$

$$\delta\rho_3 = (\delta\theta_3)' - \rho_2\delta\theta_1 + \rho_1\delta\theta_2, \tag{18}$$

where $(\delta\theta_i)'$ can be obtained using Eq. (16) and $(\delta u)' = \delta u'$, $(\delta v)' = \delta v'$, $(\delta w)' = \delta w'$, $(\delta u')' = \delta u''$, $(\delta v')' = \delta v''$ and $(\delta w')' = \delta w''$. Moreover, $(\delta\phi)' = \delta\phi'$ because ϕ is a rotation angle with respect to the ξ-axis.

3. Total-Lagrangian finite-element formulation

The principle of virtual work states that (Washizu, 1982)

$$\delta\pi = \delta W_{\mathrm{nc}}, \tag{19}$$

where Π denotes the elastic energy and W_{nc} denotes the non-conservative energy due to external distributed and/or concentrated loads.

3.1. Elastic energy

To fully account for geometric nonlinearities, we use Jaumann strains because they are fully nonlinear, objective, and geometric strain measures and their directions are defined with respect to the local coordinate system $\xi\eta\zeta$ (Pai and Palazotto, 1995a). The movement of a cross section consists of two parts. The first part is due to rigid-body displacements u, v, and w of the reference point and the rotation angle ϕ (see Fig. 1). This rigid-body motion rotates the sides dy and dz of the observed cross section so that they are parallel to the η- and ζ-axes, respectively. The second part is due to a local, strainable displacement vector **U**, which consists of relative displacements with respect to the local coordinate system $\xi\eta\zeta$. Because the rigid-body motion does not result in any strain energy, to calculate the elastic energy we only need to deal with the strainable, local displacement field **U**. This local displacement field can be represented as

$$\mathbf{U} = u_1\mathbf{i}_1 + u_2\mathbf{i}_2 + u_3\mathbf{i}_3$$

$$u_1(s, y, z) = u_1^0(s) + z[\theta_2(s) - \theta_{20}(s)] - y[\theta_3(s) - \theta_{30}(s)] + \gamma_6 y + \gamma_5 z,$$

$$u_2(s, y, z) = u_2^0(s) - z[\theta_1(s) - \theta_{10}(s)]$$

$$u_3(s, y, z) = u_3^0(s) + y[\theta_1(s) - \theta_{10}(s)]. \tag{20}$$

Here, the Lagrangian coordinates s, y and z are used to express all functions because Jaumann strains are defined using the undeformed length. Moreover, u_1, u_2 and u_3 are local, strainable displacements with respect to the ξ-, η- and ζ-axes, respectively; $u_i^0(s) \equiv u_i(s, 0, 0)$, $i = 1, 2, 3$; θ_1, θ_2 and θ_3 are the rotation angles of the observed cross section with respect to the ξ-, η- and ζ-axes, respectively; and θ_{10}, θ_{20} and θ_{30} are the initial rotation angles of the observed cross section with respect to the ξ-, η- and ζ-axes, respectively. Moreover, γ_5 and γ_6 are the energy-averaged shear rotation angles (Pai and Schulz, 1999) at the reference point with respect to the y- and $-z$-axes, respectively.

Because the system $\xi\eta\zeta$ is a local coordinate system attached to the observed cross section and the unit vector $\mathbf{i}_1$ is tangent to the deformed reference axis, we have

$$u_i^0 = \theta_{i0} = \theta_i = \frac{\partial u_2^0}{\partial s} = \frac{\partial u_3^0}{\partial s} = 0,\ e = \frac{\partial u_1^0}{\partial s},\ \rho_i = \frac{\partial \theta_i}{\partial s},\ k_i = \frac{\partial \theta_{i0}}{\partial s},\ i = 1, 2, 3. \tag{21}$$

It follows from Eqs. (20), (21), (13a), and (13b) that

$$\frac{\partial \mathbf{U}}{\partial s} = \left[e + z(\rho_2 - k_2) - y(\rho_3 - k_3) + \gamma_6' y + \gamma_5' z\right]\mathbf{i}_1 + [-z(\rho_1 - k_1) + y\rho_3\gamma_6 + z\rho_3\gamma_5]\mathbf{i}_2 + [y(\rho_1 - k_1) - y\rho_2\gamma_6 - z\rho_2\gamma_5]\mathbf{i}_3,$$

$$\frac{\partial \mathbf{U}}{\partial y} = \gamma_6\mathbf{i}_1$$

$$\frac{\partial \mathbf{U}}{\partial z} = \gamma_5\mathbf{i}_1. \tag{22}$$

Without performing any complex polar decomposition (Malvern, 1969; Pai and Palazotto, 1995a), Jaumann strains can be derived by using the local displacement field as

$$B_{11} = \frac{\partial \mathbf{U}}{\partial s} \cdot \mathbf{i}_1 = e + z(\rho_2 - k_2) - y(\rho_3 - k_3) + \gamma_6' y + \gamma_5' z,$$

$$B_{12} = \frac{\partial \mathbf{U}}{\partial s} \cdot \mathbf{i}_2 + \frac{\partial \mathbf{U}}{\partial y} \cdot \mathbf{i}_1 = -z(\rho_1 - k_1) + (1 + y\rho_3)\gamma_6 + z\rho_3\gamma_5$$

$$B_{13} = \frac{\partial \mathbf{U}}{\partial s} \cdot \mathbf{i}_3 + \frac{\partial \mathbf{U}}{\partial z} \cdot \mathbf{i}_1 = y(\rho_1 - k_1) - y\rho_2\gamma_6 + (1 - z\rho_2)\gamma_5. \tag{23}$$

This strain–displacement relation can be put in the following matrix form.

$$\begin{Bmatrix} B_{11} \\ B_{12} \\ B_{13} \end{Bmatrix} = [S]\{\psi\}, \tag{24}$$

where

$$\{\psi\} = \left\{e, \gamma_6, \gamma_5, \rho_1 - k_1, \rho_2 - k_2, \rho_3 - k_3, \gamma_6', \gamma_5'\right\}^T \tag{25a}$$

$$[S] = \begin{bmatrix} 1 & 0 & 0 & 0 & z & -y & y & z \\ 0 & 1+yk_3 & zk_3 & -z & 0 & 0 & 0 & 0 \\ 0 & -yk_2 & 1-zk_2 & y & 0 & 0 & 0 & 0 \end{bmatrix}. \tag{25b}$$

Here, we replace ρ_3 and ρ_2 with k_3 and k_2 in Eq. (25b) to simplify the derivation. For thick beams, curvatures will not have significant changes before failure. For thin beams, curvatures may have significant changes before failure, but their shear deformations, γ_5 and γ_6, are negligible. Hence, this approximation will not cause a significant loss in accuracy. The stress–strain relation can be obtained as (Whitney, 1987)

$$\begin{Bmatrix} J_{11} \\ J_{12} \\ J_{13} \end{Bmatrix} = [\bar{Q}]\begin{Bmatrix} B_{11} \\ B_{12} \\ B_{13} \end{Bmatrix}, [\bar{Q}] = \begin{bmatrix} \bar{Q}_{11} & \bar{Q}_{16} & \bar{Q}_{15} \\ \bar{Q}_{61} & \bar{Q}_{66} & \bar{Q}_{65} \\ Q_{51} & Q_{56} & Q_{55} \end{bmatrix}, \tag{26}$$

where $[\bar{Q}]$ is a 3×3 symmetric matrix reduced from the transformed material stiffness matrix using the assumption $J_{22} = J_{33} = J_{23} = 0$.

Using Eq. (26), we obtain that

$$\delta\Pi = \int_0^L \int_A (J_{11}\delta B_{11} + J_{12}\delta B_{12} + J_{13}\delta B_{13})\mathrm{d}A\ \mathrm{d}s = \int_0^L \int_A \{\delta B\}^T[\bar{Q}]\{B\}\mathrm{d}A\ \mathrm{d}s, \tag{27}$$

where A denotes the undeformed area of the cross section and L is the beam length. Substituting Eq. (24) into Eq. (27) yields

$$\delta\Pi = \int_0^L \{\delta\psi\}^T[\Phi]\{\psi\}\mathrm{d}s, \tag{28}$$

where $[\Phi]$ is an 8×8 symmetric matrix given by

$$[\Phi] = \int_A [S]^T[\bar{Q}][S]\mathrm{d}A. \tag{29}$$

The entries of $[\Phi]$ are given in Appendix A. In a formulation that accounts for three-dimensional stress effects due to in-plane and out-of-plane warpings (Pai and Nayfeh, 1994b), the expressions of $\{\psi\}$ and $\delta\Pi$ are the same as Eqs. (25a) and (28), but the matrix $[\Phi]$ needs to be obtained using two-dimensional sectional analyses (e.g., Giavotto et al., 1983).

It follows from Eqs. (25a) and (16)–(18), that

$$\{\delta\psi\} = [\Psi]\{\delta U\}, \tag{30}$$

where

$$\{U\} = \left\{u, u', u'', v, v', v'', w, w', w'', \phi, \phi', \gamma_5, \gamma_5', \gamma_6, \gamma_6'\right\}^T. \tag{31}$$

The entries Ψ_{ij} $(=\partial\psi_i/\partial U_j)$ of $[\Psi]$ are given in Appendix B. Substituting Eq. (30) into Eq. (28) yields

$$\delta\Pi = \int_0^L \{\delta U\}^T[\Psi]^T[\Phi]\{\psi\}\mathrm{d}s. \tag{32}$$

The way that the components of $\{U\}$ are approximated defines the type of a specific finite element. Using the finite-element discretization scheme, we discretize the displacements as

$$\{u, v, w, \phi, \gamma_5, \gamma_6\}^T = [N]\{q^{[j]}\}, \tag{33}$$

where $\{q^{[j]}\}$ is the nodal displacement vector of the jth element and $[N]$ is a matrix of one-dimensional finite-element interpolation or shape functions, which are in terms of natural coordinates. To keep the virtual rotations continuous, it follows from Eq. (16) that u', as well as v' and w', need to be continuous. Hence, we choose

$$\begin{aligned}\{q^{[j]}\} = \Big\{ & u^{(j)}, v^{(j)}, w^{(j)}, \phi^{(j)}, w'^{(j)}, v'^{(j)}, u'^{(j)}, \gamma_5^{(j)}, \gamma_6^{(j)} u^{(j+1)}, v^{(j+1)}, w^{(j+1)}, \phi^{(j+1)}, w'^{(j+1)}, \\ & v'^{(j+1)}, u'^{(j+1)}, \gamma_5^{(j+1)}, \gamma_6^{(j+1)} \Big\}^T,\end{aligned} \tag{34}$$

where $u^{(m)}$ denotes the displacement component u of the mth global node and two-node elements are assumed to be used. Comparing with linear finite-element models of beams in three-dimensional space that account for shear deformations, u' is the only additional degree of freedom used at each node in this nonlinear model. Numerical experience shows that the use of u' increases the element size that can converge in incremental/iterative solution procedures. The reason is that the use of u' ensures the continuity of rotations at each node because $[T]$ (see Eqs. (9) and (10)) is a function of u' as well as v' and w'. Substituting Eq. (33) into Eq. (31) yields

$$\{U\} = [D]\{q^{[j]}\}, \quad [D] \equiv [\partial][N], \tag{35}$$

where $[D]$ is a 15×18 matrix, $[N]$ is a 6×18 matrix, and $[\partial]$ is a 15×6 matrix consisting of partial differentiation operators. Substituting Eq. (35) into Eq. (32) yields

$$\delta\Pi = \sum_{j=1}^{N_e} \int_{L^{[j]}} \{\delta q^{[j]}\}^T[D]^T[\Psi]^T[\Phi]\{\psi\}\mathrm{d}s = \sum_{j=1}^{N_e} \{\delta q^{[j]}\}^T[K^{[j]}]\{q^{[j]}\} = \{\delta q\}^T[K]\{q\}, \tag{36}$$

where

$$[K^{[j]}]\{q^{[j]}\} \equiv \int_{L^{[j]}} [D]^T[\Psi]^T[\Phi]\{\psi\}\mathrm{d}s. \tag{37}$$

N_e is the total number of elements, $L^{[j]}$ is the length of the jth element, $[K^{[j]}]$ is the stiffness matrix of the jth element, $[K]$ is the structural (global) stiffness matrix, and $\{q\}$ is the structural (global) displacement vector. We note that $[K^{[j]}]$ is not explicitly written and may be asymmetric.

The governing equations need to be linearized and solved by incremental/iterative methods because the structural stiffness matrix is a nonlinear function of displacements. To derive linearized incremental equations, we let

$$\{q^{[j]}\} = \{q^0\} + \{\Delta q^{[j]}\}$$

$$\{U\} = \{U^0\} + \{\Delta U\}, \tag{38}$$

where $\{q^0\}$ denotes the equilibrium solution and $\{\Delta q^{[j]}\}$ the increment displacement vector. Then, we obtain the first-order expansions of $\{\psi\}$ and $[\Psi]$ as

$$\{\psi\} = \{\psi^0\} + [\Psi^0]\{\delta U\} \tag{39}$$

$$[\Psi] = [\Psi^0] + [\Xi], \tag{40}$$

where the entry Ξ_{ij} of $[\Xi]$ is given by

$$\Xi_{ij} = \frac{\partial^2 \psi_i}{\partial U_j \partial U_k} \Delta U_k. \tag{41}$$

Then, we use Eqs. (39) and (40) to expand Eq. (37) into

$$[K^{[j]}]\{q^{[j]}\} = \int_{L^{[j]}} \left[[D]^T [\Psi^0]^T [\Phi]\{\psi^0\} + [D]^T [\Psi^0]^T [\Phi][\Psi^0]\{\Delta U\} + [D]^T [\Xi]^T [\Phi]\{\psi^0\} \right] \mathrm{d}s. \tag{42}$$

Using Eq. (41) and $[\Phi] = [\Phi]^T$, one can prove that

$$[\Xi]^T [\Phi]\{\psi^0\} = [\Upsilon]\{\Delta U\}, \tag{43}$$

where $[\Upsilon]$ is a symmetric matrix and its entry, Υ_{ij}, is given by

$$\Upsilon_{ij} = \Upsilon_{ji} = \psi_m^0 \Phi_{mn} \frac{\partial^2 \psi_n^0}{\partial U_i \partial U_j} = \psi_m^0 \Phi_{mn} \frac{\partial \Psi_{ni}^0}{\partial U_j}. \tag{44}$$

Hence, substituting Eq. (43) into Eq. (42) yields

$$[K^{[j]}]\{q^{[j]}\} = [\breve{K}^{[j]}]\{\Delta q^{[j]}\} + [K^{[j]}]\{q^{[j]}\}|_{\{q^{[j]}\}=\{q^0\}}, \tag{45}$$

where $[\breve{K}^{[j]}]$ is the so-called elemental tangent stiffness matrix and is given by

$$[\breve{K}^{[j]}] = \int_{L^{[j]}} [D]^T ([\Psi^0]^T [\Phi][\Psi^0] + [\Upsilon])[D] \mathrm{d}s \tag{46}$$

$$[K^{[j]}]\{q^{[j]}\}|_{\{q^{[j]}\}=\{q^0\}} = \int_{L^{[j]}} [D]^T [\Psi^0]^T [\Phi]\{\psi^0\} \mathrm{d}s. \tag{47}$$

We note that $[\breve{K}^{[j]}]$ is a symmetric matrix.

3.2. External loads

It follows from Eqs. (16), (31) and (35) that the variation of non-conservative energy due to external loads is

$$\delta W_{\mathrm{nc}} = \int_0^L (r_1\delta u + r_2\delta v + r_3\delta w + r_4\delta\theta_1 + r_5\delta\theta_2 + r_6\delta\theta_3)\mathrm{d}s = \int_0^L \{\delta U\}^T\{\bar{R}\}\mathrm{d}s = \sum_{j=1}^{N_e}\{\delta q^{[j]}\}^T\{R^{[j]}\}$$

$$= \{\delta q\}^T\{R\}, \tag{48}$$

where r_1, r_2 and r_3 are distributed and/or concentrated external loads along the x-, y- and z-axes, respectively, and r_4, r_5 and r_6 are distributed and/or concentrated twisting and bending moments. The entries of $\{\bar{R}\}$ are shown in Appendix C, $\{R^{[j]}\}$ is the elemental nodal loading vector, and $\{R\}$ is the structural nodal loading vector. Furthermore,

$$\{R^{[j]}\} \equiv \int_{L^{[j]}} [D]^T\{\bar{R}\}\mathrm{d}s. \tag{49}$$

Because $\delta\theta_i$ are nonlinear functions of displacements, parametric loadings exist when finite rotations are involved.

3.3. Incremental-iterative solution method

An incremental/iterative method is used to solve the derived nonlinear governing equations. With the use of a loading parameter λ, the governing equation of a static problem can be stated as

$$[K]\{q\} = \lambda\{R_r\}, \tag{50}$$

where $\{R_r\}$ is a reference load vector. Let

$$\{q\} \equiv \{q\}_i = \{q^0\} + \{\Delta q\}_i = \{q\}_{i-1} + \{\delta q\}_i \tag{51a}$$

$$\lambda \equiv \lambda_i = \lambda^0 + \Delta\lambda_i = \lambda_{i-1} + \delta\lambda_i, \tag{51b}$$

where $i \geq 2$, i is the number of iterations in searching for a converged solution when the load increases from $\lambda = \lambda^0$ to $\lambda = \lambda^0 + \delta\lambda_i$, $\{q^0\}$ denotes the equilibrium solution corresponding to $\lambda = \lambda^0$, $\{q\}_i$ denotes the iterated estimated solution corresponding to $\lambda = \lambda_i$, and $\{\Delta q\}_i$ denotes the incremental displacement vector corresponding to the increment $\Delta\lambda_i = \lambda_i - \lambda^0$ of the loading parameter. Substituting Eqs. (51a) and (51b) into Eq. (50), expanding the result into a Taylor series and neglecting higher-order terms, we obtain

$$[\hat{K}]_{i-1}\{\delta q\}_i = \delta\lambda_i\{R_r\}_{i-1} + \{g\}_{i-1}, \tag{52}$$

where

$$\{g\}_{i-1} \equiv \lambda_{i-1}\{R_r\}_{i-1} - ([K]\{q\})_{i-1}$$

$$[\hat{K}]_{i-1} \equiv [\breve{K}]_{i-1} - \lambda_{i-1}[\bar{K}]_{i-1}. \tag{53}$$

Here $[\bar{K}]$ is due to parametric loadings (some examples are shown in Section 5), $[\hat{K}]_{i-1}$ is the total tangent stiffness matrix, and the subindecies indicate the state, e.g., $[\hat{K}]_{i-1} \equiv [\hat{K}]_{\{q\}} = \{q\}_{i-1}$, $\lambda = \lambda_{i-1}$. To obtain $\{\delta q\}_i$ and λ_i, we use an alternative version of Riks' method (Lee, 1992; Riks, 1979) to solve Eq. (52) and a constraint equation

$$\{\Delta q\}_{i-1}^T\{\delta q\}_i + \Delta\lambda_{i-1}\delta\lambda_i\{R_r\}_{i-1}^T\{R_r\}_{i-1} = 0, \tag{54}$$

which limits the arc-length increment by confining the current searching direction to be perpendicular to the previous accumulated searching direction (Riks, 1979).

4. Experimental set-ups

The flexibility of HFSs makes it difficult to measure displacements by conventional means. For example, any indicator that carries a small spring force does not supply accurate readings because the spring force results in a significant structural deformation. Electronic strain gages change the structural stiffness, and they cannot reveal rigid-body deformations because they only measure relative straining displacements. Air gages apply a force to the structure and deform the structure significantly. Laser gauging is an option because it is a non-contacting method, but the equipment is expensive and it is difficult to chase the measuring point when large rotations are involved. Several of these methods were evaluated, based on the goal of measuring large deformations of beams and frames, and some of them were actually tried. We finally decided to build different fixtures for bending and twisting tests.

4.1. Bending tests

For bending tests, we built an accurate reference metal frame that can be used to fix the test structure and to measure three-dimensional displacements from the frame, as shown in Fig. 2. The two circular slots on the vertical wall can be used to fix the beam root fixture at different angles and hence different loading conditions can be tested. Choosing an appropriate instrument to take the readings is another challenging issue. A vernier scale was chosen in the beginning, but its resolution is only 0.0078 in and it is difficult to judge the instruments proximity to the structure. If the instrument does not contact the structure and a sight of some kind is used, parallax is a problem. We chose to use a dial caliper with a brass probe mounted on the tip, a series circuit, and an indicator lamp to ascertain the immediate contact of the probe and the structure. In measuring displacements, the probe is slowly moved toward the structure until the lamp lights.

4.2. Twisting tests

For twisting tests, we built a fixture that is convenient for applying large torsional loads, as shown in

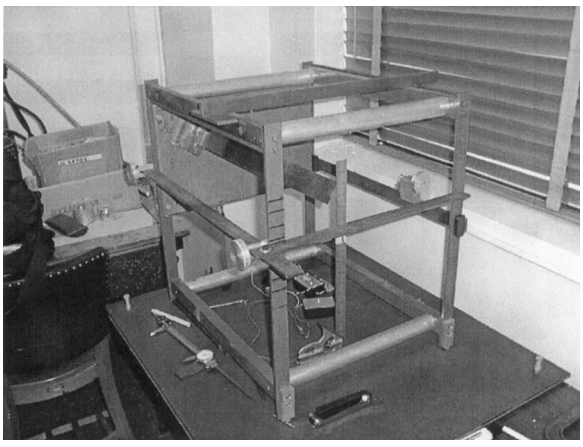

Fig. 2. The set-up for bending tests.

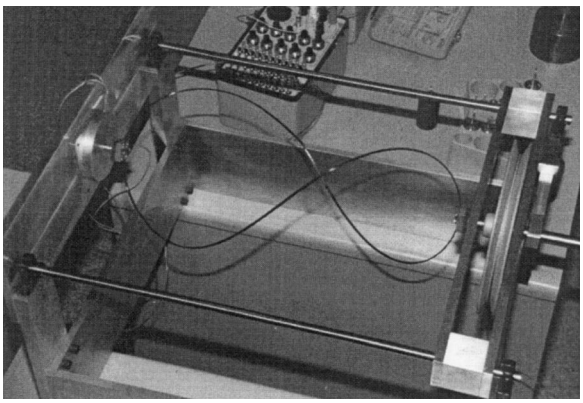

Fig. 3. The set-up for twisting tests.

Fig. 3 with a circular band twisted about its diameter. The fixture consists of a rigid base, two parallel rods, and a carriage that slides on the rods with bearings. The carriage can be locked at any location along the rods. A shaft is mounted in the middle of the carriage on precision bearings. A clamp is fixed to the rigid base and grips the circular band. Another clamp is fixed on one end of the shaft. These two clamps are designed to allow the band to deflect as freely as possible. A pulley is fixed in the middle of the shaft and provides a moment to the band when weights are hung from a cable that wraps around the pulley. A lever arm with a one-way clutch goes on the other end of the shaft. The one-way clutch allows the shaft to turn in only one direction. The moment caused by the weight of the lever arm is accounted for in the measurements.

5. Numerical and experimental results

5.1. Bending of a cantilevered isotropic beam

For an initially straight cantilever beam subjected to an end bending moment M_2 with respect to the y-axis (see Fig. 4), we have $v = v' = \phi = \gamma_6 = 0$ and the boundary conditions are

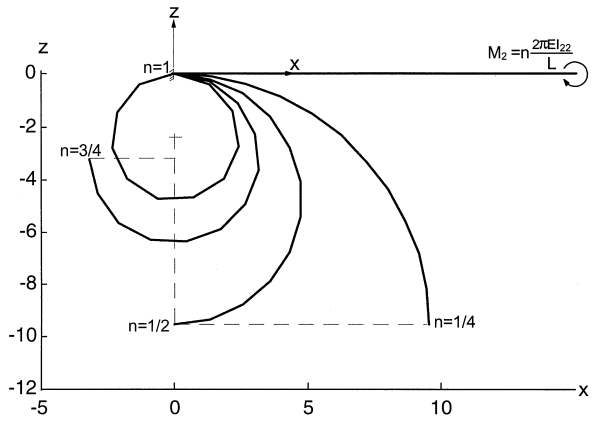

Fig. 4. A cantilevered isotropic beam subjected to an end bending moment.

$$u = v = w = \phi = w' = v' = \gamma_5 = \gamma_6 = 0 \text{ at } x = 0. \tag{55}$$

It follows from Eqs. (10)–(12) and (16) that, at the tip end (i.e., $x = L$),

$$\begin{gathered} T_{11} = T_{33} = \frac{1+u'}{1+e},\ T_{13} = -T_{31} = \frac{w'}{1+e},\ T_{12} = 0,\ 1+e = \sqrt{(1+u')^2 + w'^2},\ \theta = \cos^{-1} T_{11}, \\ M_2 \delta\theta_2 = M_2 \left[\frac{w'}{(1+u')^2 + w'^2} \delta u' - \frac{1+u'}{(1+u')^2 + w'^2} \delta w' \right], \end{gathered} \tag{56}$$

where θ denotes the tip rotation angle. Hence, the non-zero entries of $\{R^{[N_e]}\}$ are

$$R_{14}^{[N_e]} = \frac{-\hat{M}_2(1+u')}{(1+u')^2 + w'^2},\ R_{16}^{[N_e]} = \frac{\hat{M}_2 w'}{(1+u')^2 + w'^2}, \tag{57}$$

where $\hat{M}_2$ is a chosen reference twisting moment and the actual twisting moment is M_2 and $M_2 = \lambda \hat{M}_2$. Moreover, the non-zero entries of $[\bar{K}^{[N_e]}]$ are

$$\bar{K}_{14,\,14}^{[N_e]} = -\bar{K}_{16,\,16}^{[N_e]} = \frac{2\hat{M}_2 w'(1+u')}{[(1+u')^2 + w'^2]^2},\ \bar{K}_{14,\,16}^{[N_e]} = \bar{K}_{16,\,14}^{[N_e]} = \frac{\hat{M}_2[(1+u')^2 - w'^2]}{[(1+u')^2 + w'^2]^2}. \tag{58}$$

We note that Eqs. (56)–(58) are given here only to show an example of $[\bar{K}]$ in Eq. (53). Users do not need to provide or derive such equations in order to use the finite-element code because the variations of $\bar{R}_i$ in Eq. (C1) are also computed by the code. Users only need to provide the geometric boundary conditions (e.g., Eq. (55)), which are the same as those used in linear finite-element analysis.

The beam is modeled using 11 equal elements with the shear correction factor $c_2 = 0.83333$ (see Appendix A). Fig. 4 shows that the deformed configurations are circular arcs, as predicted by theory. Here EI_{22} denotes the bending stiffness with respect to the y-axis. The exact load-deflection (M_2–θ_2) curve is a straight line, and the finite-element solution agrees closely with the exact solution.

5.2. Flexure of cantilevered composite beams

We consider the 56 cm × 3 cm laminated composite cantilevered beam tested by Minguet and Dugundji (1990). The beam is modeled using 11 elements (10 × 5 cm + 1 × 6 cm (free end)), and the properties of the graphite–epoxy plies are:

$E_{11} = 142$ GPa	$E_{22} = 9.8$ GPa	$E_{33} = 9.8$ GPa
$\nu_{12} = 0.3$	$\nu_{13} = 0.3$	$\nu_{23} = 0.35$
$G_{12} = 6$ GPa	$G_{13} = 6$ GPa	$G_{23} = 3.63$ GPa
Layer thickness = 0.124 mm.		

The shear correction factors (see Appendix A) can be obtained to be $c_1 = c_2 = 0.83333$, $c_3 = 0$ and $c_4 = 0.00958$ for the $[0^\circ/90^\circ]_{3s}$ beam, and $c_1 = 0.83333$, $c_2 = 0.498$, $c_3 = 1$ and $c_4 = 0.00958$ for the $[45^\circ/0^\circ]_{3s}$ beam (Pai and Schulz, 1999).

Fig. 5 shows the displacements u, v and w (along the x-, y- and z-axes) of Node 11 (at s = 50 cm) of a $[0^\circ/90^\circ]_{3s}$ beam, and Fig. 6 shows the displacements of Node 11 of a $[45^\circ/0^\circ]_{3s}$ beam. Because of the symmetric layup with angle plies, the displacement v in Fig. 6 (perpendicular to the loading plane) occurs due to bending–torsion coupling. These numerical results agree closely with the experimental results of Minguet and Dugundji (1990). However, for the $[45^\circ/0^\circ]_{3s}$ beam, there is a significant

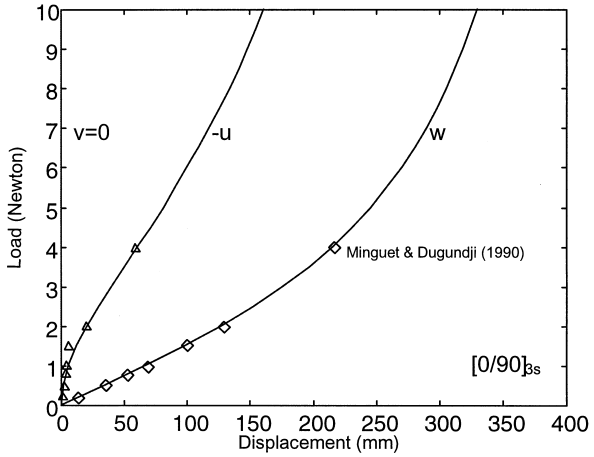

Fig. 5. The displacements of Node 11 (at $s = 50$ cm) of a $[0°/90°]_{3s}$ beam.

difference between the measured and theoretical values of u. Minguet and Dugundji (1990) directly solved a set of fully nonlinear governing equations using a finite-difference method and their solution for u has the same difference between the measured and theoretical values. Although Minguet and Dugundji (1990) did not fully account for transverse shear deformations in their numerical solutions, we found that transverse shear deformations are negligible for this specific thin beam. Hence, we suspect that there are some measuring errors or manufacturing defects in the test specimen.

5.3. Flexure of a cantilevered isotropic beam

To test large deformations of flexible beams without concerning manufacturing defects too much, we chose to test a very flexible $15'' \times 2'' \times 0.02''$ spring steel cantilever beam. Since the Young's modulus E was not known, we measured the mass density ρ to be $\rho = 0.271$ lb/in^3. Then we performed a linear vibration test to obtain natural frequencies by using a modal hammer, a proximity sensor, and a DP420

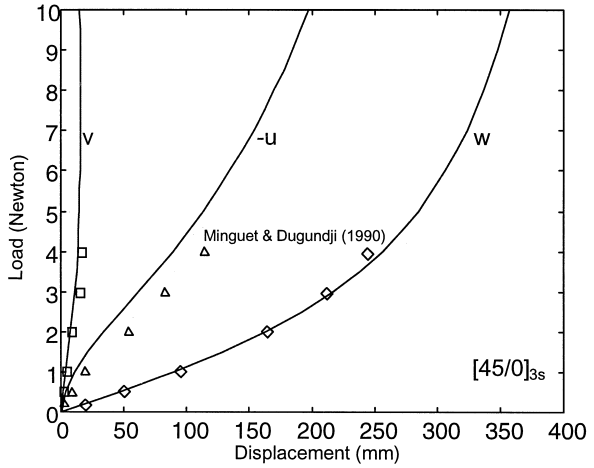

Fig. 6. The displacements of Node 11 (at $s = 50$ cm) of a $[45°/0°]_{3s}$ beam.

FFT analyzer to obtain a Frequency Response Function (FRF). Using the derived mass density, the first few natural frequencies from the measured FRF, and the formula of linear natural frequencies of a cantilever beam, we obtain that $E = 2.84 \times 10^7$ psi.

The displacements were measured at fifteen locations in 1″ increments along the beam. Measurements were taken from the metal frame (see Fig. 2) to each point on the reference line of the beam using the modified dial caliper. Initial displacements due to imperfection in the sample were measured and recorded. Then load was applied in increments of 10 g up to a maximum of 100 g. For each load, longitudinal, horizontal, and vertical displacements with respect to the metal frame were measured, and then displacements u, v and w with respect to the beam coordinate system xyz are obtained using coordinate transformation. Three different measurements were taken and the results were averaged. The displacements due to imperfection were subtracted from the averaged displacements of each point under each load.

Fig. 7(a) shows the load–deflection curves when the root fixture is fixed at zero degree, where symbols denote experimental data and solid lines are finite-element solutions using eleven equal beam elements and $c_1 = c_2 = 0.83333$, $c_3 = 0$ and $c_4 = 0.0004$. Fig. 7(b) shows the deformed geometry when the applied transverse end load is 0.22 lbf. Influence of transverse shear deformations was investigated in the finite element analysis. It was found that transverse shear deformations are negligible for this thin flexible beam.

Fig. 8 shows the numerical and experimental load–deflection curves with the root fixture fixed at different angles. The no-load deflection is due to gravity. We note that the finite-element results agree closely with the experimental results.

5.4. Twisting of an isotropic circular band

To test large torsional deformations of beams, we chose to test a circular band twisted by an angle θ at one end of a diameter and an angle $-\theta$ at the other end with the distance between these two ends being fixed, as shown in Fig. 9. The band is made of a $48.69'' \times 0.212'' \times 0.028''$ straight steel strip by welding its two ends together, and hence the radius is $r = 7.75''$. The Young's modulus and mass density are experimentally obtained to be $E = 2.276 \times 10^7$ psi and $\rho = 0.2507$ lb/in^3. The shear correction factors (see Appendix A) are calculated to be $c_1 = c_2 = 0.8333$, $c_3 = 0$, and $c_4 = 0.0617$.

Because of the symmetry of the structure and the antisymmetry of the applied moment, only one quarter of the ring needs to be modeled. The initial curvatures are $k_1 = k_3 = 0$ and $k_2 = 1/r$. The boundary conditions are

$$u = v = w = \phi = \gamma_5 = w' = 0 \text{ at } \alpha = 0^\circ$$

$$u = v = \phi = \gamma_5 = w' = 0 \text{ at } \alpha = 90^\circ. \tag{59}$$

It follows from Eqs. (59) and (10)–(12) that, at the two ends where the twisting moment M_3 is applied,

$$\begin{aligned} &T_{11} = T_{22} = \frac{1+u'}{1+e},\ T_{12} = -T_{21} = \frac{v'}{1+e},\ T_{13} = 0,\ 1+e = \sqrt{(1+u')^2 + v'^2},\ \theta = \cos^{-1} T_{11}, \\ &M_3 \delta\theta_3 = M_3 \left[\frac{-v'}{(1+u')^2 + v'^2} \delta u' + \frac{1+u'}{(1+u')^2 + v'^2} \delta v' \right]. \end{aligned} \tag{60}$$

Hence, the non-zero entries of $\{R^{[1]}\}$ are

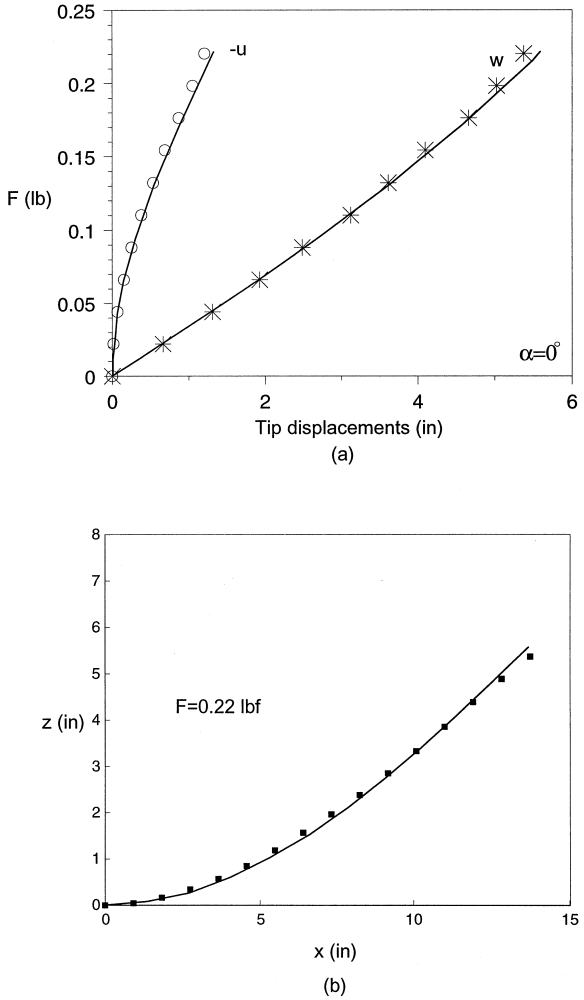

Fig. 7. Deformation of a cantilevered beam subjected to an end load with the root fixture fixed at 0°: (a) load–deflection curves, and (b) the deformed configuration when $F = 0.22$ lbf.

$$R_6^{[1]} = \frac{\hat{M}_3(1+u')}{(1+u')^2+v'^2},\ R_7^{[1]} = \frac{-\hat{M}_3 v'}{(1+u')^2+v'^2}, \tag{61}$$

where $\hat{M}_3$ is a chosen reference twisting moment and the actual twisting moment is M_3 and $M_3 = \lambda \hat{M}_3$. Moreover, the non-zero entries of $[\bar{K}^{[1]}]$ are

$$\bar{K}_{66}^{[1]} = -\bar{K}_{77}^{[1]} = \frac{-2\hat{M}_3 v'(1+u')}{[(1+u')^2+v'^2]^2},\ \bar{K}_{67}^{[1]} = \bar{K}_{76}^{[1]} = \frac{\hat{M}_3[v'^2-(1+u')^2]}{[(1+u')^2+v'^2]^2}. \tag{62}$$

We note again that users of this finite-element code only need to provide the geometric boundary conditions in Eq. (59), not those in Eqs. (60)–(62).

A special test sequence was used in using the set-up shown in Fig. 3 because the load–deflection has both positive (stable) and negative (unstable) slopes. In the regions of negative slope we could not apply

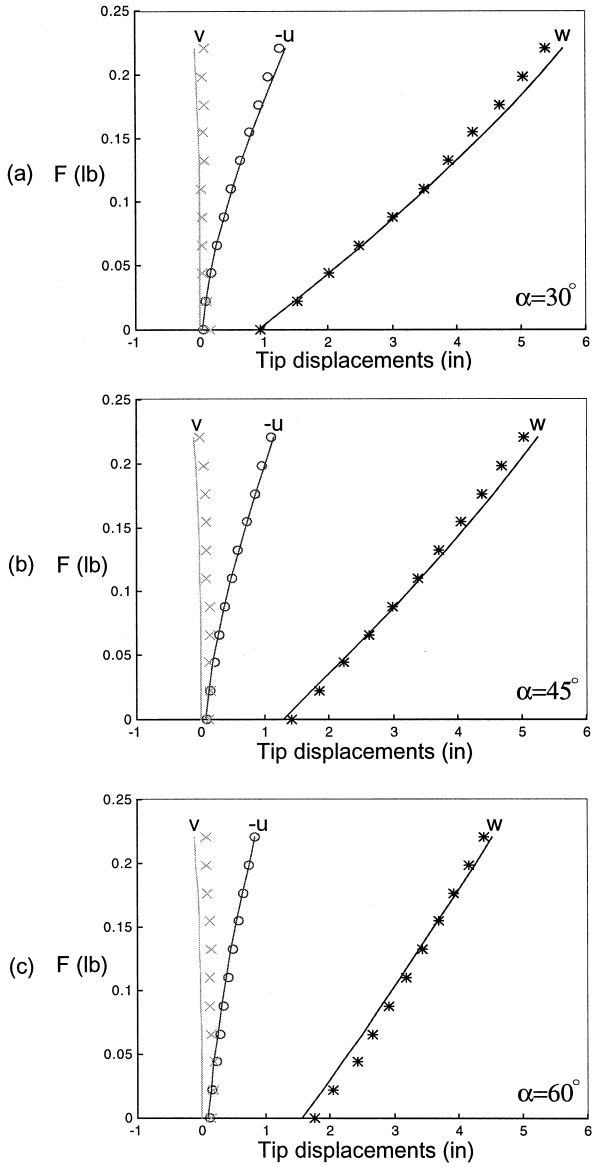

Fig. 8. Load–deflection curves of the tip point of the cantilevered beam with the root fixture fixed at: (a) 30°, (b) 45° and (c) 60°.

a moment then measure the angle because the system is unstable. Hence an angle was set first, and then weights were applied to the pulley cable until a slight gap was observed between the lever arm and the stop. The actual load at the angle setting was between the load that caused the gaping and the next lower load. This bracketed the load to within 0.022 lb (10 g). This lead to a moment resolution of 0.0827 lbf—in. We made these measurements at approximately 10° intervals over the total relative twist $2\theta = 360°$. Even with considerable care in the manufacturing and building of the set-up shown in Fig. 3, the test fixture is not perfect. There are three effects that need to be accounted for in correcting the

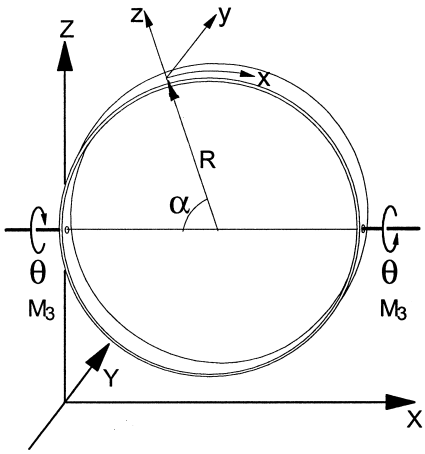

Fig. 9. A circular band is twisted through an angle of θ at both ends of a diameter, where the distance between these two ends is fixed.

measured data. One is the bearing friction that is equivalent to a nearly constant 0.1593 lbf—in. Another is an unbalance in the pulley, which changes as the applied angle changes. This requires a correction of $0.2036\sin(2\theta-20^\circ)$ lbf—in. A third correction accounts for the length of cable that hangs from pulley, which increases linearly with the applied angle. This correction is 0.04779θ lbf—in.

Fig. 10 shows the obtained normalized load–deflection curve, where gravity is neglected. A multiple shooting method (Pai and Palazotto, 1996) is also used to solve this problem. Although transverse shear deformations are neglected in the solution using the multiple shooting method, the solution still can be considered to be numerically exact because shear deformations are found in the finite-element analysis to be negligible for this thin isotropic beam. The difference between the numerical and experimental results is significant when θ is close to 180°. We note that, when the load is released in the experiment, the band springs back to its original shape with a bit of detectable asymmetric permanent deformation due to yielding. The asymmetry is due to yielding near the welded end that is gripped by one of the clamps. The plastic deformation began approximately at $\theta=150^\circ$, which was not accounted for in this nonlinear elastic analysis. Fig. 11 shows the solutions of deformed curvatures using the multiple shooting method (thick lines) and the finite-element method (thin lines). We note that the deformed twisting curvature ρ_1 is high, especially at $\alpha=0^\circ$, 90° and 180°. Because of the large twisting curvature at $\alpha=0^\circ$, the use of linear shape functions (see Eqs. (33) and (34)) for ϕ limits the sizes of elements. It also explains why the result of using 26 non-uniform elements is better than that of using 30 uniform elements in Fig. 10. Results also show that the finite-element solution in Fig. 11 can be improved by using finer elements around the loading end.

Fig. 12 shows the experimental deformed configurations corresponding to different twisting angles. The left end was fixed and the right end was rotated from 0° to 360°. The pictures were taken from the top of the set-up. Fig. 13 shows the front, top, side, and three-dimensional views of the finite-element solution of the deformed half band when $\theta=170^\circ$, which are close to that in Fig. 12 for $2\theta=330^\circ$. In general the finite-element solutions agree closely with the experimental results.

6. Concluding remarks

A total-Lagrangian displacement-based finite-element model of general anisotropic beams undergoing

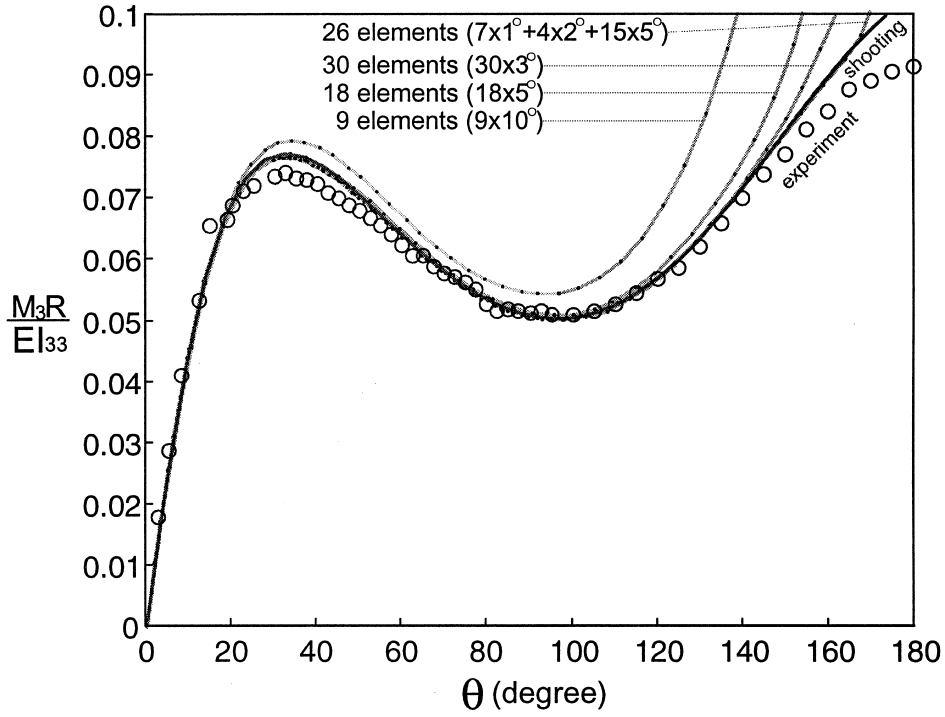

Fig. 10. The load–deflection curve of the circular band.

large displacements and rotations is derived. Large bending and twisting tests on flexible straight and curved beams have been performed. The finite-element results agree closely with the experimental results. However, to fully verify the finite-element model tests on other different beams are necessary, especially flexible composite beams with elastic bending–torsion and extension–torsion couplings. Analysis of frame structures is currently under study, which requires matching the transformation matrices $[T]$ of two adjacent beam elements at the connecting node.

Appendix A

$$[\Phi] = \int_A [S]^T[\bar{Q}][S]\mathrm{d}A, \tag{A1}$$

$$[S]^T[\bar{Q}][S] = \begin{bmatrix} \bar{Q}_{11} & \bar{Q}_{16} & \bar{Q}_{15} & R_1 & z\bar{Q}_{11} & -y\bar{Q}_{11} & y\bar{Q}_{11} & z\bar{Q}_{11} \\ & c_1\bar{Q}_{66} & c_3\bar{Q}_{56} & R_2 & z\bar{Q}_{16} & -y\bar{Q}_{16} & y\bar{Q}_{16} & z\bar{Q}_{16} \\ & & c_2\bar{Q}_{55} & R_3 & z\bar{Q}_{15} & -y\bar{Q}_{15} & y\bar{Q}_{15} & z\bar{Q}_{15} \\ & & & c_4(yR_3 - zR_2) & zR_1 & -yR_1 & yR_1 & zR_1 \\ & & & & z^2\bar{Q}_{11} & -yz\bar{Q}_{11} & yz\bar{Q}_{11} & z^2\bar{Q}_{11} \\ & & & & & y^2\bar{Q}_{11} & -y^2\bar{Q}_{11} & -yz\bar{Q}_{11} \\ & \text{sym.} & & & & & y^2\bar{Q}_{11} & yz\bar{Q}_{11} \\ & & & & & & & z^2\bar{Q}_{11} \end{bmatrix} +$$

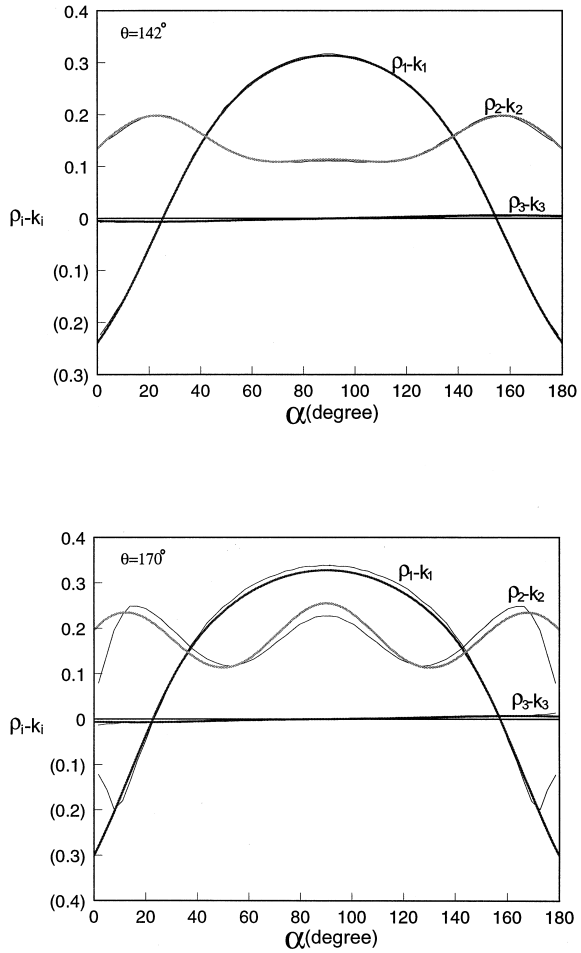

Fig. 11. The distributions of deformed curvatures of the circular band: (a) when $\theta = 142^\circ$, and (b) when $\theta = 170^\circ$ (thick lines are solutions using the multiple shooting method, and thin lines are solutions using the finite element method).

$$
\begin{bmatrix}
0 & R_4 & R_5 & 0 & 0 & 0 & 0 & 0 \\
 & c_1(2R_6 + yk_3R_6 - yk_2R_8) & c_3(R_7 + R_8 + yk_3R_7 - yk_2R_9) & yR_8 - zR_6 & zR_4 & -yR_4 & yR_4 & zR_4 \\
 & & c_2(2R_9 + zk_3R_7 - zk_2R_9) & yR_9 - zR_7 & zR_5 & -yR_5 & yR_5 & zR_5 \\
 & & & 0 & 0 & 0 & 0 & 0 \\
 & & & & 0 & 0 & 0 & 0 \\
 & & & & & 0 & 0 & 0 \\
 & \text{sym.} & & & & & 0 & 0 \\
 & & & & & & & 0
\end{bmatrix}
$$

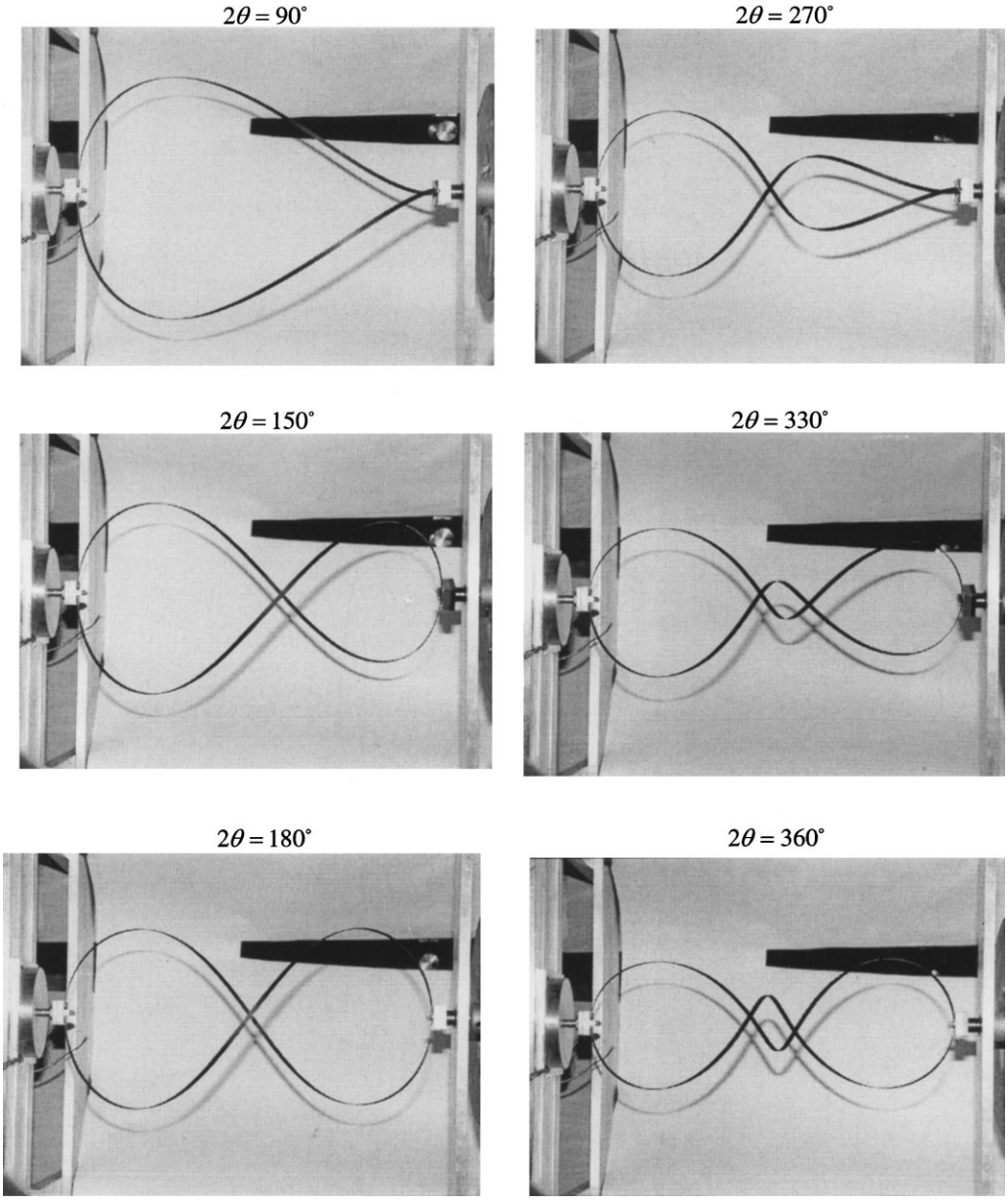

Fig. 12. Experimental deformed geometries of the circular band at different total twisting angle 2θ: (a) $2\theta = 90°$, (b) $2\theta = 150°$, (c) $2\theta = 180°$, (d) $2\theta = 270°$, (e) $2\theta = 330°$ and (f) $2\theta = 360°$.

$$
\begin{aligned}
&R_1 \equiv y\bar{Q}_{15} - z\bar{Q}_{16},\ R_2 \equiv y\bar{Q}_{56} - z\bar{Q}_{66},\ R_3 \equiv y\bar{Q}_{55} - z\bar{Q}_{56},\ R_4 \equiv y\left(k_3\bar{Q}_{16} - k_2\bar{Q}_{15}\right),\\
&R_5 \equiv z\left(k_3\bar{Q}_{16} - k_2\bar{Q}_{15}\right),\ R_6 \equiv y\left(k_3\bar{Q}_{66} - k_2\bar{Q}_{56}\right),\ R_7 \equiv z\left(k_3\bar{Q}_{66} - k_2\bar{Q}_{56}\right),\\
&R_8 \equiv y\left(k_3\bar{Q}_{56} - k_2\bar{Q}_{55}\right),\ R_9 \equiv z\left(k_3\bar{Q}_{56} - k_2\bar{Q}_{55}\right).
\end{aligned}
\tag{A2}
$$

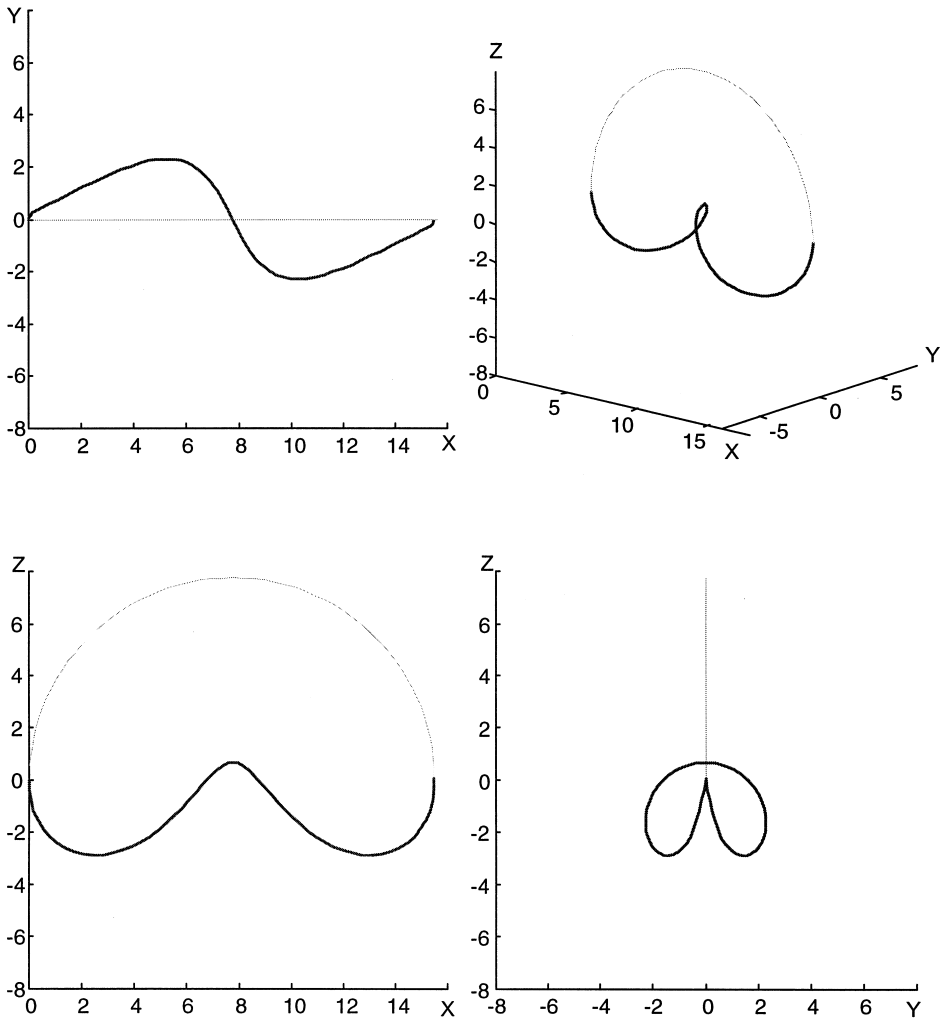

Fig. 13. Different views of the finite-element solution of the deformed geometry of the half circular band twisted by $\theta = 170^\circ$ at both ends (thin curves represent the undeformed geometry).

Here, c_1, c_2 and c_3 are shear correction factors used to account for the higher-order effects due to warpings, c_4 is used to account for the higher-order effects on the torsional rigidity (Timoshenko and Goodier, 1970), and the influences of higher-order effects on other rigidities are neglected. The shear correction factors can be calculated using an energy-equivalent first-order shear-deformation theory (Pai and Schulz, 1999).

Appendix B

Using Eqs. (17), (18) and (16) and the fact that $\delta\psi_i = \partial\psi_i/\partial U_j \delta U_j = \Psi_{ij}\delta U_j$, we obtain the following non-zero elements of $[\Psi]$. Here, we use two digits to represent one subindex number of Ψ_{ij}. For example, $\Psi_{ij}|_{i=1,\, j=2}$ is represented by Ψ_{0102}.

$$\Psi_{0101} = T_{12}k_3 - T_{13}k_2,$$

$$\Psi_{0102} = T_{11},$$

$$\Psi_{0104} = T_{13}k_1 - T_{11}k_3,$$

$$\Psi_{0105} = T_{12},$$

$$\Psi_{0107} = T_{11}k_2 - T_{12}k_1,$$

$$\Psi_{0108} = T_{13},$$

$$\Psi_{0401} = \left(\frac{T_{13}k_3 + T_{12}k_2}{1+e+T_{11}+eT_{11}}\right)' + \frac{T_{22}k_3 - T_{23}k_2}{1+e}\rho_2 - \frac{T_{33}k_2 - T_{32}k_3}{1+e}\rho_3,$$

$$\Psi_{0402} = \frac{T_{21}\rho_2 + T_{31}\rho_3}{1+e} + \frac{T_{13}k_3 + T_{12}k_2}{1+e+T_{11}+eT_{11}},$$

$$\Psi_{0404} = -\left(\frac{T_{12}k_1}{1+e+T_{11}+eT_{11}}\right)' + \frac{T_{23}k_1 - T_{21}k_3}{1+e}\rho_2 - \frac{T_{31}k_3 - T_{33}k_1}{1+e}\rho_3,$$

$$\Psi_{0405} = \frac{T_{22}\rho_2 + T_{32}\rho_3}{1+e} - \frac{T_{12}k_1}{1+e+T_{11}+eT_{11}} + \left(\frac{T_{13}}{1+e+T_{11}+eT_{11}}\right)',$$

$$\Psi_{0406} = \frac{T_{13}}{1+e+T_{11}+eT_{11}},$$

$$\Psi_{0407} = -\left(\frac{T_{13}k_1}{1+e+T_{11}+eT_{11}}\right)' + \frac{T_{21}k_2 - T_{22}k_1}{1+e}\rho_2 - \frac{T_{32}k_1 - T_{31}k_2}{1+e}\rho_3,$$

$$\Psi_{0408} = \frac{T_{23}\rho_2 + T_{33}\rho_3}{1+e} - \frac{T_{13}k_1}{1+e+T_{11}+eT_{11}} - \left(\frac{T_{12}}{1+e+T_{11}+eT_{11}}\right)',$$

$$\Psi_{0409} = -\frac{T_{12}}{1+e+T_{11}+eT_{11}},$$

$$\Psi_{0411} = 1,$$

$$\Psi_{0501} = \left(\frac{T_{33}k_2 - T_{32}k_3}{1+e}\right)' + \frac{T_{13}k_3 + T_{12}k_2}{1+e+T_{11}+eT_{11}}\rho_3 - \frac{T_{22}k_3 - T_{23}k_2}{1+e}\rho_1,$$

$$\Psi_{0502} = -\frac{T_{21}\rho_1}{1+e} + \frac{T_{33}k_2 - T_{32}k_3}{1+e} - \left(\frac{T_{31}}{1+e}\right)',$$

$$\Psi_{0503} = -\frac{T_{31}}{1+e},$$

$$\Psi_{0504} = \left(\frac{T_{31}k_3 - T_{33}k_1}{1+e}\right)' - \frac{T_{12}k_1}{1+e+T_{11}+eT_{11}}\rho_3 - \frac{T_{23}k_1 - T_{21}k_3}{1+e}\rho_1,$$

$$\Psi_{0505} = \frac{T_{13}\rho_3}{1+e+T_{11}+eT_{11}} - \frac{T_{22}\rho_1}{1+e} + \frac{T_{31}k_3 - T_{33}k_1}{1+e} - \left(\frac{T_{32}}{1+e}\right)',$$

$$\Psi_{0506} = -\frac{T_{32}}{1+e},$$

$$\Psi_{0507} = \left(\frac{T_{32}k_1 - T_{31}k_2}{1+e}\right)' - \frac{T_{13}k_1}{1+e+T_{11}+eT_{11}}\rho_3 - \frac{T_{21}k_2 - T_{22}k_1}{1+e}\rho_1,$$

$$\Psi_{0508} = -\frac{T_{12}\rho_3}{1+e+T_{11}+eT_{11}} - \frac{T_{23}\rho_1}{1+e} + \frac{T_{32}k_1 - T_{31}k_2}{1+e} - \left(\frac{T_{33}}{1+e}\right)',$$

$$\Psi_{0509} = -\frac{T_{33}}{1+e},$$

$$\Psi_{0510} = \rho_3,$$

$$\Psi_{0601} = \left(\frac{T_{22}k_3 - T_{23}k_2}{1+e}\right)' - \frac{T_{13}k_3 + T_{12}k_2}{1+e+T_{11}+eT_{11}}\rho_2 + \frac{T_{33}k_2 - T_{32}k_3}{1+e}\rho_1,$$

$$\Psi_{0602} = -\frac{T_{31}\rho_1}{1+e} + \frac{T_{22}k_3 - T_{23}k_2}{1+e} + \left(\frac{T_{21}}{1+e}\right)',$$

$$\Psi_{0603} = \frac{T_{21}}{1+e},$$

$$\Psi_{0604} = \left(\frac{T_{23}k_1 - T_{21}k_3}{1+e}\right)' + \frac{T_{12}k_1}{1+e+T_{11}+eT_{11}}\rho_2 + \frac{T_{31}k_3 - T_{33}k_1}{1+e}\rho_1,$$

$$\Psi_{0605} = -\frac{T_{13}\rho_2}{1+e+T_{11}+eT_{11}} - \frac{T_{32}\rho_1}{1+e} + \frac{T_{23}k_1 - T_{21}k_3}{1+e} + \left(\frac{T_{22}}{1+e}\right)',$$

$$\Psi_{0606} = \frac{T_{22}}{1+e},$$

$$\Psi_{0607} = \left(\frac{T_{21}k_2 - T_{22}k_1}{1+e}\right)' + \frac{T_{13}k_1}{1+e+T_{11}+eT_{11}}\rho_2 + \frac{T_{32}k_1 - T_{31}k_2}{1+e}\rho_1,$$

$$\Psi_{0608} = \frac{T_{12}\rho_2}{1+e+T_{11}+eT_{11}} - \frac{T_{33}\rho_1}{1+e} + \frac{T_{21}k_2 - T_{22}k_1}{1+e} + \left(\frac{T_{23}}{1+e}\right)',$$

$$\Psi_{0609} = \frac{T_{23}}{1+e},$$

$$\Psi_{0610} = -\rho_2,$$

$$\Psi_{0214} = 1,$$

$$\Psi_{0312} = 1,$$

$$\Psi_{0715} = 1$$

$$\Psi_{0813} = 1, \tag{B1}$$

where

$$e' = T_{11}\left(u'' - v'k_3 - vk_3' + w'k_2 + wk_2'\right) + T_{12}\left(v'' + u'k_3 + uk_3' - w'k_1 - wk_1'\right) + T_{13}\left(w'' - u'k_2 - uk_2' + v'k_1 + vk_1'\right) \tag{B2}$$

$$\begin{bmatrix} T_{11}' & T_{12}' & T_{13}' \\ T_{21}' & T_{22}' & T_{23}' \\ T_{31}' & T_{32}' & T_{33}' \end{bmatrix} = [K][T] - [T][k]. \tag{B3}$$

Eq. (B2) is obtained by using Eqs. (10) and (11), and Eq. (B3) is obtained by post-multiplying Eq. (13b) by $[T]$ and using the identity $[T]^T = [T]^{-1}$.

Appendix C

The non-zero entries of $\{\bar{R}\}$ in Eq. (48) are given below:

$$\bar{R}_1 = r_1 + r_4\frac{T_{13}k_3 + T_{12}k_2}{1+e+T_{11}+eT_{11}} + r_5\frac{T_{33}k_2 - T_{32}k_3}{1+e} + r_6\frac{T_{22}k_3 - T_{23}k_2}{1+e},$$

$$\bar{R}_2 = -r_5\frac{T_{31}}{1+e} + r_6\frac{T_{21}}{1+e},$$

$$\bar{R}_4 = r_2 - r_4\frac{T_{12}k_1}{1+e+T_{11}+eT_{11}} + r_5\frac{T_{31}k_3 - T_{33}k_1}{1+e} + r_6\frac{T_{23}k_1 - T_{21}k_3}{1+e},$$

$$\bar{R}_5 = r_4\frac{T_{13}}{1+e+T_{11}+eT_{11}} - r_5\frac{T_{32}}{1+e} + r_6\frac{T_{22}}{1+e},$$

$$\bar{R}_7 = r_3 - r_4\frac{T_{13}k_1}{1+e+T_{11}+eT_{11}} + r_5\frac{T_{32}k_1 - T_{31}k_2}{1+e} + r_6\frac{T_{21}k_2 - T_{22}k_1}{1+e},$$

$$\bar{R}_8 = -r_4\frac{T_{12}}{1+e+T_{11}+eT_{11}} - r_5\frac{T_{33}}{1+e} + r_6\frac{T_{23}}{1+e}$$

$$\bar{R}_{10} = r_4. \tag{C1}$$

References

Alkire, K., 1984. An Analysis of Rotor Blade Twist Variables Associated With Different Euler Sequences and Pretwist Treatments NASA TM 84394.

Giavotto, V., Borri, M., Mantegazza, P., Ghiringhelli, G., Carmaschi, V., Maffioli, G.C., Mussi, F., 1983. Anisotropic beam theory and applications. Computers & Structures 16, 403–413.

Kohnke, P.C. (Ed.), 1989. Engineering Analysis System — Theoretical Manual for ANSYS Revision 4.4. Swanson Analysis Systems, Inc, Houston, Pennsylvania.

Lee, S.H. (Ed.), 1992. MSC/NASTRAN Handbook for Nonlinear Analysis, Version 67. The MacNeal–Schwendler Corporation.

Malvern, L.E., 1969. Introduction to the Mechanics of a Continuous Medium. Prentice–Hall, Inc, Englewood Cliffs, New Jersey.

Minguet, P., Dugundji, J., 1990. Experiments and analysis for composite blades under large deflections. Part I. Static behavior. AIAA Journal 28, 1573–1579.

Nygard, M.K., Bergan, P.G., 1989. Advances in treating large rotations for nonlinear problems. In: Noor, A.K., Oden, J.T. (Eds.), State-of-The-Art Surveys on Computational Mechanics. American Society of Mechanical Engineers, pp. 305–333.

Pai, P.F., 1995. A new look at shear correction factors and warping functions of anisotropic laminates. Int. J. Solids and Structures 32, 2295–2313.

Pai, P.F., Nayfeh, A.H., 1991. A nonlinear composite plate theory. Nonlinear Dynamics 2, 445–477.

Pai, P.F., Nayfeh, A.H., 1992. Fully nonlinear model of cables. AIAA Journal 30, 2993–2996.

Pai, P.F., Nayfeh, A.H., 1994a. A new method for the modeling of geometric nonlinearities in structures. Computers & Structures 53, 877–895.

Pai, P.F., Nayfeh, A.H., 1994b. A fully nonlinear theory of curved and twisted composite rotor blades accounting for warpings and three-dimensional stress effects. Int. J. Solids and Structures 31, 1309–1340.

Pai, P.F., Nayfeh, A.H., 1994c. A unified nonlinear formulation for plate and shell theories. Nonlinear Dynamics 6, 459–500.

Pai, P.F., Palazotto, A.N., 1995a. Polar decomposition theory in nonlinear analyses of solids and structures. J. Engineering Mechanics 121 (4), 568–581.

Pai, P.F., Palazotto, A.N., 1995b. Nonlinear displacement-based finite-element analysis of composite shells — A new total Lagrangian formulation. Int. J. Solids and Structures 32, 3047–3073.

Pai, P.F., Palazotto, A.N., 1996. Large-deformation analysis of flexible beams. Int. J. Solids and Structures 33, 1335–1353.

Pai, P.F., Palazotto, A.N., Greer, J.M., 1998. Polar decomposition and appropriate strains and stresses for nonlinear structural analyses. Computers & Structures 66 (6), 823–840.

Pai, P.F., Schulz, M.J., 1999. Shear correction factors and an energy-consistent beam theory. Int. J. Solids and Structures 36, 1523–1540.

Palazotto, A.N., Dennis, S.T., 1992. Nonlinear Analysis of Shell Structures. American Institute of Aeronautics and Astronautics, Inc, Washington, DC.

Rankin, C.C., Brogan, F.A., 1986. An element-independent corotational procedure for the treatment of large rotations. ASME Journal of Pressure Vessel Technology 108, 165–174.

Riks, E., 1979. An incremental approach to the solution of snapping and buckling problems. Int. J. Solids and Structures 15, 524–551.

Timoshenko, S.P., Goodier, J.N., 1970. Theory of Elasticity, 3rd ed. McGraw–Hill, New York.

Stanley, G., Nour-Omid, S., 1990. The Computational Structural Mechanics Testbed Generic Structural-Element Processor Manual, NASA Contractor Report 181728.

Surana, K.S., 1983. Geometrically nonlinear formulation for the curved shell elements. Int. J. for Numerical Methods in Engineering 19, 581–615.

Washizu, K., 1982. Variational Methods in Elasticity & Plasticity, 3rd ed. Pergamon Press Inc, New York.

Whitney, J.M., 1987. Structural Analysis of Laminated Anisotropic Plates. Technomic Publishing Company, Inc, Pennsylvania.